

## Characteristics of medium-scale traveling ionospheric disturbances observed near the Antarctic Peninsula by HF radar

A. Grocott,<sup>1</sup> K. Hosokawa,<sup>2</sup> T. Ishida,<sup>3</sup> M. Lester,<sup>1</sup> S. E. Milan,<sup>1</sup> M. P. Freeman,<sup>4</sup>  
N. Sato,<sup>3</sup> and A. S. Yukimatu<sup>3</sup>

Received 8 April 2013; revised 8 August 2013; accepted 12 August 2013; published 5 September 2013.

[1] We present a survey of medium-scale traveling ionospheric disturbances (MSTIDs) observed by a Super Dual Auroral Radar Network HF radar located in the Falkland Islands between May 2010 and April 2011. The radar has a field of view that overlooks the Antarctic Peninsula, a known hot spot of gravity wave activity. We present observations of radar ground-backscatter data, in which the signatures of MSTIDs are manifested as structured enhancements in echo power. Observed periods were in the range 30–80 min, corresponding to frequencies of 0.2–0.6 mHz. Wavelengths were generally in the range 200–800 km and phase speeds in the range 100–300 m s<sup>-1</sup>. These values are within the ranges typically associated with medium-scale gravity waves. We find a primary population of northward (equatorward) propagating MSTIDs, which demonstrate an association with enhanced solar wind-magnetosphere coupling and a smaller, westward propagating population, that could be associated with atmospheric gravity waves excited by winds over the Andean and Antarctic Peninsula mountains or by the high winds of the Antarctic Polar Vortex.

**Citation:** Grocott, A., K. Hosokawa, T. Ishida, M. Lester, S. E. Milan, M. P. Freeman, N. Sato, and A. S. Yukimatu (2013), Characteristics of medium-scale traveling ionospheric disturbances observed near the Antarctic Peninsula by HF radar, *J. Geophys. Res. Space Physics*, 118, 5830–5841, doi:10.1002/jgra.50515.

### 1. Introduction

[2] Traveling ionospheric disturbances (TIDs) are wave-like variations in ionospheric electron density with scale sizes ranging from a few hundred kilometers to over 1000 km. They tend to be categorized as either medium-scale TIDs (MSTIDs) having speeds of 100–250 m s<sup>-1</sup>, periods of 15 min to 1 h, and wavelengths of several hundred kilometers, or large-scale TIDs (LSTIDs) having speeds of 400–1000 m s<sup>-1</sup>, periods of 0.5–3 h, and wavelengths greater than 1000 km [Ogawa *et al.*, 1987]. A survey of TIDs at midlatitudes conducted at Millstone Hill using differential-Doppler measurements of Navy Navigation Series Satellite beacon waves [Evans *et al.*, 1983] found that most fell into the medium-scale category, having wavelengths in the range of 150–350 km. They were observed at all local times,

although their occurrence peaked during the daytime, as well as being higher in winter and at the equinoxes, and reduced in summer. A more recent study of global positioning system data in southern California [Kotake *et al.*, 2007] also revealed a population of daytime MSTIDs occurring in winter and at the equinoxes. Most of these MSTIDs propagated southeastward and were interpreted as signatures of atmospheric gravity waves (AGWs) in the thermosphere. In contrast, the properties of nighttime TIDs show little seasonal dependence [e.g., Shiokawa *et al.*, 2003; Otsuka *et al.*, 2004], which does not fit with the classical theory of gravity waves [Miller *et al.*, 1997; Kelley and Miller, 1997], and instead, an ionospheric plasma instability [e.g., Perkins, 1973] has been supposed as a candidate source in this case.

[3] The association between daytime MSTIDs and AGWs [e.g., Hines, 1960; Hooke, 1968; Francis, 1974; Hocke and Schlegel, 1996] makes the former a useful proxy for AGW studies. AGWs are the focus of much modern atmospheric research due to their important role in atmospheric dynamics. In particular, they significantly affect global circulation through their ability to transport and redistribute energy and momentum vertically through different layers of the atmosphere and horizontally across the globe. Considerable progress has been made recently in determining the spatial distribution and temporal variability of AGWs using satellite measurements [e.g., Ern *et al.*, 2004; Alexander *et al.*, 2008]. For example, the Andes and Antarctic Peninsula region has been identified as a global AGW hot spot with estimated

<sup>1</sup>Department of Physics and Astronomy, University of Leicester, Leicester, UK.

<sup>2</sup>Department of Communication Engineering and Informatics, University of Electro-Communications, Chofu, Tokyo, Japan.

<sup>3</sup>Space and Upper Atmospheric Science Group, National Institute of Polar Research, Tachikawa, Tokyo, Japan.

<sup>4</sup>British Antarctic Survey, Natural Environment Research Council, Cambridge, UK.

Corresponding author: A. Grocott, Department of Physics and Astronomy, University of Leicester, University Road, Leicester, LE1 7RH, UK. (a.grocott@ion.le.ac.uk)

©2013. American Geophysical Union. All Rights Reserved.  
2169-9380/13/10.1002/jgra.50515

momentum fluxes an order of magnitude greater than the global average. Satellite measurements cannot, however, yield the direction of the horizontal wave vector which is important in determining the sources and spectrum of these waves. For example, they may be directly excited by winds over the Andean and Antarctic Peninsula mountains [Alexander *et al.*, 2008], by the high winds of the Antarctic Polar Vortex [Ern *et al.*, 2004], or by disturbances at auroral latitudes associated with Lorentz forcing and Joule Heating [Chimonas and Hines, 1970]. Ground-based studies, on the other hand, have proved more successful in determining the source regions of AGWs. A study conducted at the high-latitude Syowa Station in Antarctica, for example, revealed a population of equatorward propagating daytime MSTIDs, consistent with a source in the auroral ionosphere [Ogawa *et al.*, 1987].

[4] A more recent ground-based technique for identifying and characterizing daytime MSTIDs involves the study of ground-reflected echoes from HF radars [e.g., Samson *et al.*, 1989; Bristow *et al.*, 1994; Sofko and Huang, 2000; He *et al.*, 2004]. Obliquely propagating radar signals at frequencies near 10 MHz are refracted in the ionosphere such that they return to the ground; from there, they scatter back along the propagation path and return to the radar [Milan *et al.*, 1997]. In the presence of MSTIDs, the radar signals are focused and defocused at the ionospheric reflection point, causing the power of the ground-echoes to be modulated accordingly. The modulation of ground-echo power can then be inspected for characteristic oscillations and propagation parameters determined by performing cross-spectral analysis on observations from different regions within the radar field-of-view (for further details of this as a technique for studying MSTIDs, see section 2). In a horizontally stratified medium, the wave frequency in the ground frame and the horizontal wave number are invariant with height [e.g., Eckermann, 1992]. We can therefore directly compare these radar measurements with other measurements at other altitudes, within the limitations of the radar data analysis, discussed below. However, in doing so, we must distinguish AGWs propagating upward from the troposphere from AGWs generated by variations in energy deposition at higher altitudes in the auroral zone caused by Joule heating and energetic particle precipitation [e.g., Samson *et al.*, 1990].

[5] In this paper, we exploit data from an HF radar that was located on the Falkland Islands to study the characteristics of daytime MSTIDs propagating in the vicinity of the Antarctic Peninsula. We collated statistics on MSTIDs observed over a 1 year period between May 2010 and April 2011, in an attempt to elucidate their characteristics and source mechanisms. We determined their occurrence frequency, frequency spectrum, wavelength, and propagation characteristics as well as their seasonal and diurnal variations and relationship to geomagnetic conditions. We find observed periods in the range 30–80 min (corresponding to frequencies of 0.2–0.6 mHz), wavelengths in the range 200–800 km, and phase speeds in the range 100–300 m s<sup>-1</sup>; these values are within the ranges typically associated with medium-scale gravity waves. We find a primary population of northward (equatorward) propagating MSTIDs, which demonstrates an association with solar wind-magnetosphere-ionosphere coupling and a smaller, westward propagating population, that could be associated

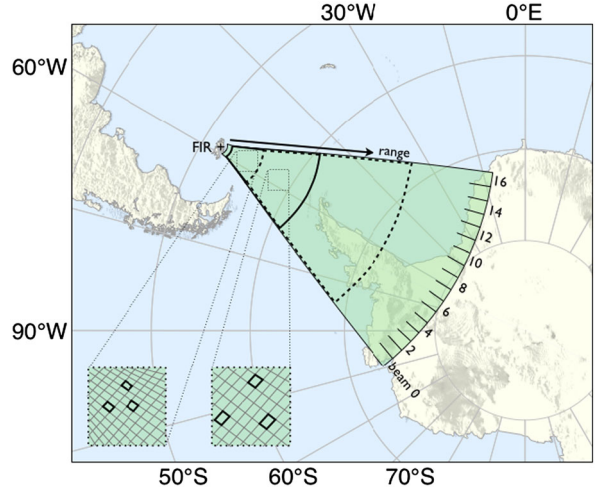


**Figure 1.** A map showing the location, at 51.8°S, 59.0°W geographic coordinates, and field-of-view (shaded green) of the Falkland Island Radar. Grey concentric circles represent lines of geographic latitude (labeled along the bottom of the figure), and radial lines represent geographic longitude (labeled along the top and to the left). The region of the field-of-view enclosed by the thick dashed line corresponds to the area of radar ground-backscatter observations indicated in Figure 5. The region enclosed by the thick solid line corresponds to this area mapped to the reflection point in the ionosphere. The numbered divisions shown along the far edge of the field-of-view indicate the different radar beam numbers; the radar field-of-view is divided into 16 beams × 75 range “cells.” Two example “3-cell sets” used in the TID analysis are shown enlarged, illustrating the convergence of the beams at near-ranges.

with AGWs excited by winds over the Andean and Antarctic Peninsula mountains or by the high winds of the Antarctic Polar Vortex.

## 2. Instrumentation and Analysis Technique

[6] We use data from an HF radar located on the Falkland Islands (hereafter referred to as the Falkland Islands Radar, or FIR) to identify traveling ionospheric disturbances. The location of the FIR (at 51.8°S, 59.0°W geographic coordinates, 37.6°S, 9.9°E geomagnetic) and its field-of-view are shown in Figure 1. The FIR is a part of the Super Dual Auroral Radar Network (SuperDARN), an international array of coherent radars in the Northern and Southern Hemispheres [Greenwald *et al.*, 1995; Chisham *et al.*, 2007]. In its normal operating mode, the radar scans through 16 beams of azimuthal separation 3.24°, with a dwell time of 3 s on each beam, thus completing a full ~52° scan in ~1 min. A transmitted pulse length of 300 μs equates to a range resolution of 45 km along each beam, with measurements from 75 range gates (spanning ~3500 km) being regularly recorded. The radar is therefore capable of measuring TIDs with wavelengths in the range ~100 to ~1000 km.

[7] The primary function of SuperDARN is to make line-of-sight velocity measurements of horizontal ionospheric motions, determined from the Doppler shift of

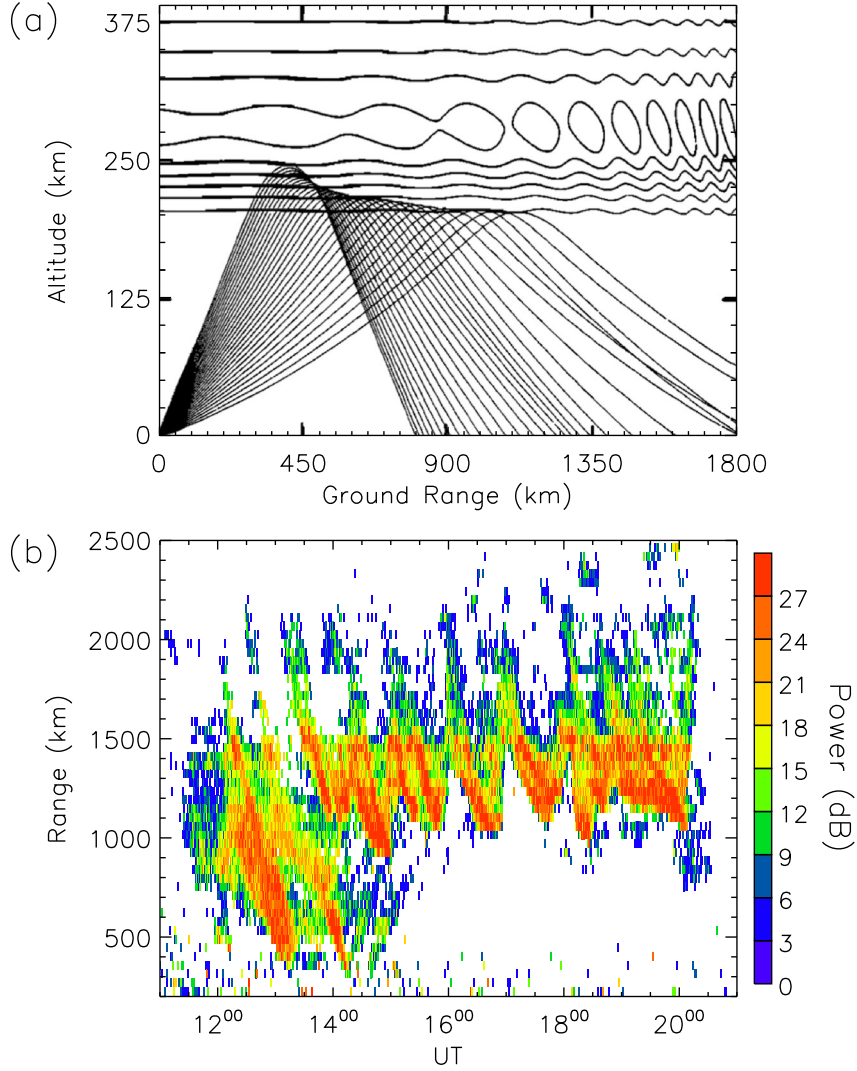


**Figure 2.** (a) Model ray paths of HF radar propagation through an ionosphere modulated by a TID. Focusing and defocusing at the ground is caused by the uneven contours of electron density (adapted from Samson *et al.* [1990]). (b) An example of the resultant FIR data, showing the ground-backscattered power received by the radar along a single beam, versus ground range and universal time.

backscatter from ionospheric plasma irregularities. In order for backscatter to be received at the radar, the radar signal must intersect the ionospheric targets orthogonally, a situation that is achieved owing to the refraction of the radar signal as it propagates in the ionosphere. If the signals are not reflected from the ionosphere, then further refraction may cause the signal to propagate back down to the ground, from which it can be backscattered and propagate back to the radar. Such ground-backscattered signals are routinely identified in the SuperDARN data by their low Doppler shift and narrow spectral width [Milan *et al.*, 1997]. The power of these ground-backscattered signals is affected by the focusing of the radar signal at the ionospheric reflection point which, for example, can be modulated by variations in electron density associated with the presence of TIDs. This process is illustrated schematically in Figure 2a. Figure 2b then shows a corresponding example of the FIR radar data that results from this process. These data were taken on an

approximately southward pointing beam (beam 8) and were received from geographic latitudes between  $\sim 55^{\circ}\text{S}$  and  $\sim 70^{\circ}\text{S}$ . The striations in ground-backscattered power that result from the ionospheric focusing of the radar signal are clearly evident.

## 2.1. Mapping of Ground Backscatter to the Ionosphere

[8] It is apparent from Figure 2a that the location of the TIDs implied from the ground range of the radar signal is displaced from the true location at the reflection point of the radar signal in the ionosphere. In order to account for this effect, we must therefore map the location of the data from its ground range,  $R$ , to an estimate of the distance to the ionospheric reflection point,  $D$ . It is also clear that the nature of this mapping will impact the subsequent determination of the horizontal wavelength and propagation speed, and so due consideration should be given to the mapping applied. A number of previous authors have discussed

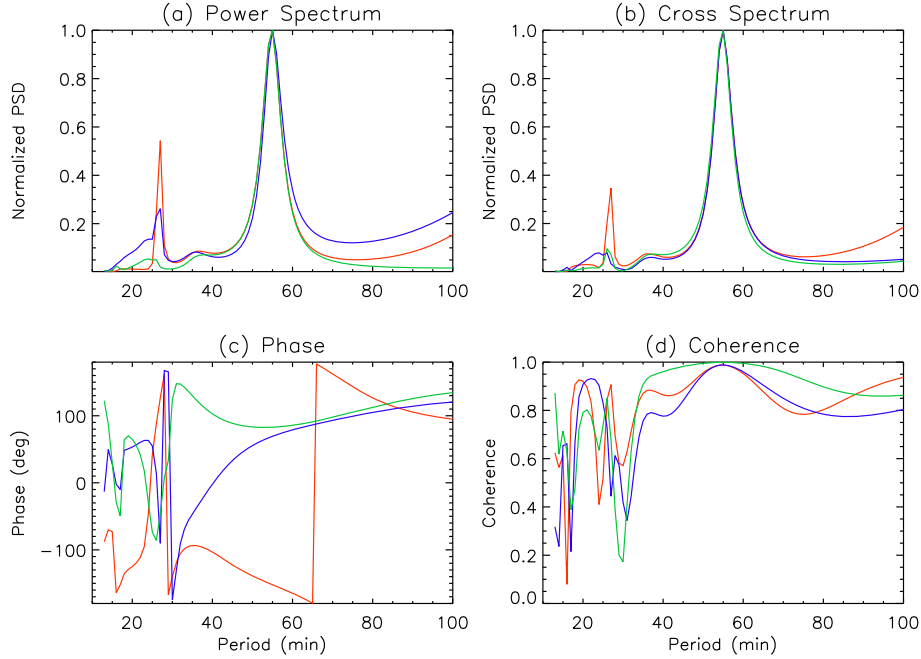


**Figure 3.** An example of the spectra used in the MULMEM analysis, for a 160 s spectral window centered at 1640 UT, on 4 August 2010. (a) Power spectrum of the time series at each of the three cells  $C(b, r) = C_0(0, 29)$  (red),  $C_1(2, 25)$  (blue), and  $C_2(4, 29)$  (green). (b–d) Cross spectrum, phase, and coherence calculated for each pair of cells  $(C_1, C_0)$  (red),  $(C_2, C_1)$  (blue), and  $(C_0, C_2)$  (green), respectively.

this mapping, which we consider briefly here. *Bristow et al.*, [1994] treated the ionosphere like a horizontal mirror, leading to the following relation:

$$D = R_e \sin^{-1} \left[ \frac{\sqrt{R^2/4 - h^2}}{R_e} \right], \quad (1)$$

where  $R_e$  is the radius of the Earth and  $h$  is an assumed reflection height of 300 km. *He et al.* [2004] used a simpler mapping of  $D = 0.5R$ , and *Hall et al.* [1999] suggested a mapping, supported by ray tracing, that indicated  $D$  values of  $\sim 0.6R$ . HF ray tracing and MSTID modeling by *MacDougall et al.* [2001] even suggested that the factor  $D/R$  could be close to 1.0, although *Hall et al.* [1999] points out such an extreme case is likely to hold only for very large amplitude TIDs. *MacDougall et al.* [2001] were modeling their TIDs on data from the Saskatoon SuperDARN radar, located much closer to the auroral oval than the FIR and where the amplitudes of the TIDs would therefore be expected to be higher. To investigate the consequences of this uncertainty, we performed our analysis, described below, with a number of different mappings. Ultimately, we consider the mapping used by *Hall et al.* [1999] to be the most appropriate choice. Nevertheless, we discuss the effects of the different mappings on our results in section 4.

## 2.2. MSTID Analysis Method

[9] The propagation parameters of MSTIDs are found using an algorithm that determines their period and phase

velocity from the normal-mode SuperDARN observations [*Ishida et al.*, 2008]. The algorithm is based on cross-spectral analysis using the multichannel maximum entropy method (MULMEM) [*Shibata*, 1987; *Strand*, 1977; *Ulrych and Bishop*, 1975] and is performed using a 160 min data window, shifted dynamically over the data interval under investigation. As MSTIDs typically have a wave period of 20–50 min, a data window of 160 min covers at least 3–4 wave periods. On each day, the length of the data interval is chosen according to the coverage of the radar ground-backscatter data (see section 3.1), which varies between a minimum of 4 h and a maximum of 12 h. The algorithm takes three sets of time series ground-backscattered power data, obtained at three radar “cells” to enable a two-dimensional determination of the phase velocity. As MSTIDs typically have wavelengths of a few hundred kilometers, a cell separation of 50–100 km was used. Two such “3-cell sets” are shown enlarged in Figure 1. In the right-hand example, the separation in range is four cells, corresponding to 180 km at the ground ( $4 \times 45$  km range gate separation) and  $\sim 100$  km at the ionospheric reflection point. Owing to the beam geometry, the range separation was decreased from four gates to two gates at ground-ranges within 1000 km (illustrated in the left-hand example), to account for the convergence of the beams and maintain a quasi-constant equilateral separation of the three cells. This results in a minimum cell separation of 90 km at the ground and  $\sim 50$  km at the ionospheric reflection point.

[10] The full array of beam-range combinations,  $C(b, r)$ , used to form the unique observation sets can be summarized as follows:

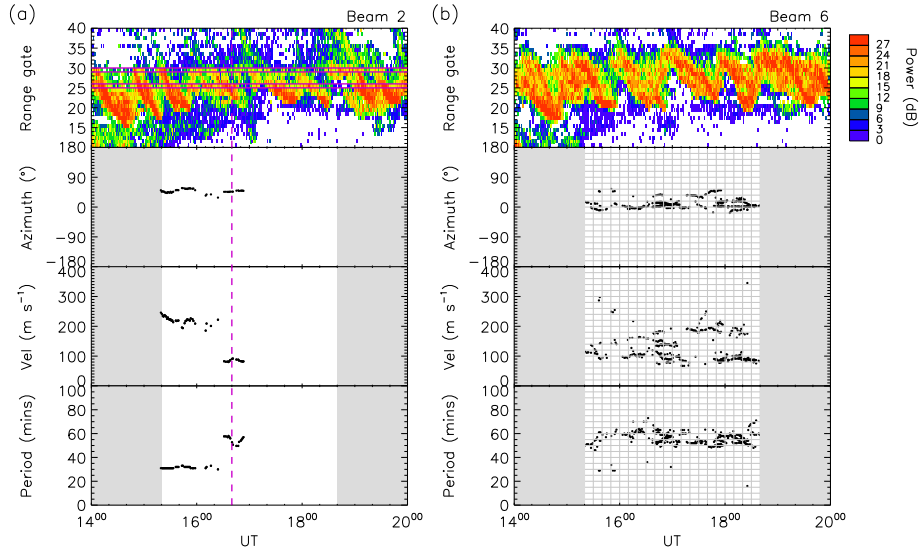


**Figure 4.** Two example sets of MSTID observations from 14 to 20 UT on 4 August 2010. The first panel presents the backscattered power from the central beam of the radar cells used in the MULMEM analysis, and the second, third, and fourth panels present the propagation azimuth, velocity, and wave period, respectively, determined for each spectral window. A point on the graph corresponds to the central time of each window; the grey-shaded regions indicate the outside of these center-times. In Figure 4a, the results from a single 3-cell set are shown, with the corresponding cell range gates indicated by the horizontal magenta lines and the data from Figure 3 indicated by the vertical dashed line. In Figure 4b, the results from all 3-cell sets are shown, illustrating the grouping of observations into different time-parameter bins (grey grid) discussed in the text.

$$\begin{aligned}
 C(b, r) &= [(b-2, r), (b, r+2), (b+2, r)] \\
 &\quad \text{for } 2 \leq b \leq 13 \text{ and } 10 \leq r \leq 21 \\
 C(b, r) &= [(b-2, r), (b, r+4), (b+2, r)] \\
 &\quad \text{for } 2 \leq b \leq 13 \text{ and } 22 \leq r \leq 37 \\
 C(b, r) &= [(b-2, r+2), (b, r), (b+2, r+2)] \\
 &\quad \text{for } 2 \leq b \leq 13 \text{ and } 10 \leq r \leq 18 \\
 C(b, r) &= [(b-2, r+4), (b, r), (b+2, r+4)] \\
 &\quad \text{for } 2 \leq b \leq 13 \text{ and } 19 \leq r \leq 32,
 \end{aligned}$$

where the choice of radar range limits imposed was determined according to the nature of the radar ground-backscatter (discussed in section 3.1) and the range at which the distortion of the 3-cell symmetry (caused by the beam convergence discussed above) was minimized. In total, this results in  $12 \times 51 (= 612)$  beam-range combinations that were systematically inspected for MSTID signatures. The use of multiple observation sets maximizes the probability of an MSTID propagating somewhere within the radar field-of-view being captured. Rather than determining an average over the range and time interval of the measurements, we analyze the different cross-spectra to reveal the spatial and temporal distribution of the MSTID characteristics. This is elaborated on below.

[11] An illustration of the results of the MULMEM analysis is shown in Figure 3. Figure 3a shows the power spectrum of the time series at each of the three cells  $C(b, r) = C_0(0, 29)$ ,  $C_1(2, 25)$ , and  $C_2(4, 29)$ , shown in red, blue, and green, respectively. Figure 3b shows the cross spectrum, Figure 3c the phase, and Figure 3d the coherence, calculated

for each pair of cells  $(C_1, C_0)$  (red),  $(C_2, C_1)$  (blue), and  $(C_0, C_2)$  (green). In this example, the dominant period can be identified at 55 mins. Cases where the dominant period varied between the reference cells by more than 5 mins, or where the peak coherence was less than 0.8, were excluded. The horizontal phase velocity is then obtained from the phase and distances between each pair of reference cells calculated using spherical trigonometry. This analysis is repeated over an extended interval of data to build up a picture of the temporal evolution of the MSTID parameters. An example data set, from 4 August 2010, is presented in Figure 4a, with the data from Figure 3 indicated by the vertical dashed magenta line. The first panel presents the backscattered power from the central beam of the three radar cells, from 14 to 20 UT in this case, with the corresponding range gates indicated by the horizontal magenta lines. The second, third, and fourth panels present the propagation azimuth (defined such that geographic north is  $0^\circ$ , east is  $+90^\circ$ ), velocity, and wave period, respectively, as determined for each spectral window. A point on the graph corresponds to the central time of the window, thus MULMEM data are only shown between 15:20 and 18:40 UT; regions outside these times are shaded grey. Where no data point is present within the white areas, this indicates that the MULMEM analysis failed to return a result, for reasons described above. The results in Figure 4a show that two distinct disturbances were identified; data in the fourth panel reveal an interval in which a  $\sim 30$  min period disturbance was observed, followed by the identification of a second longer period disturbance. This is also apparent from the spacing between the echo power enhancements shown in the first panel.

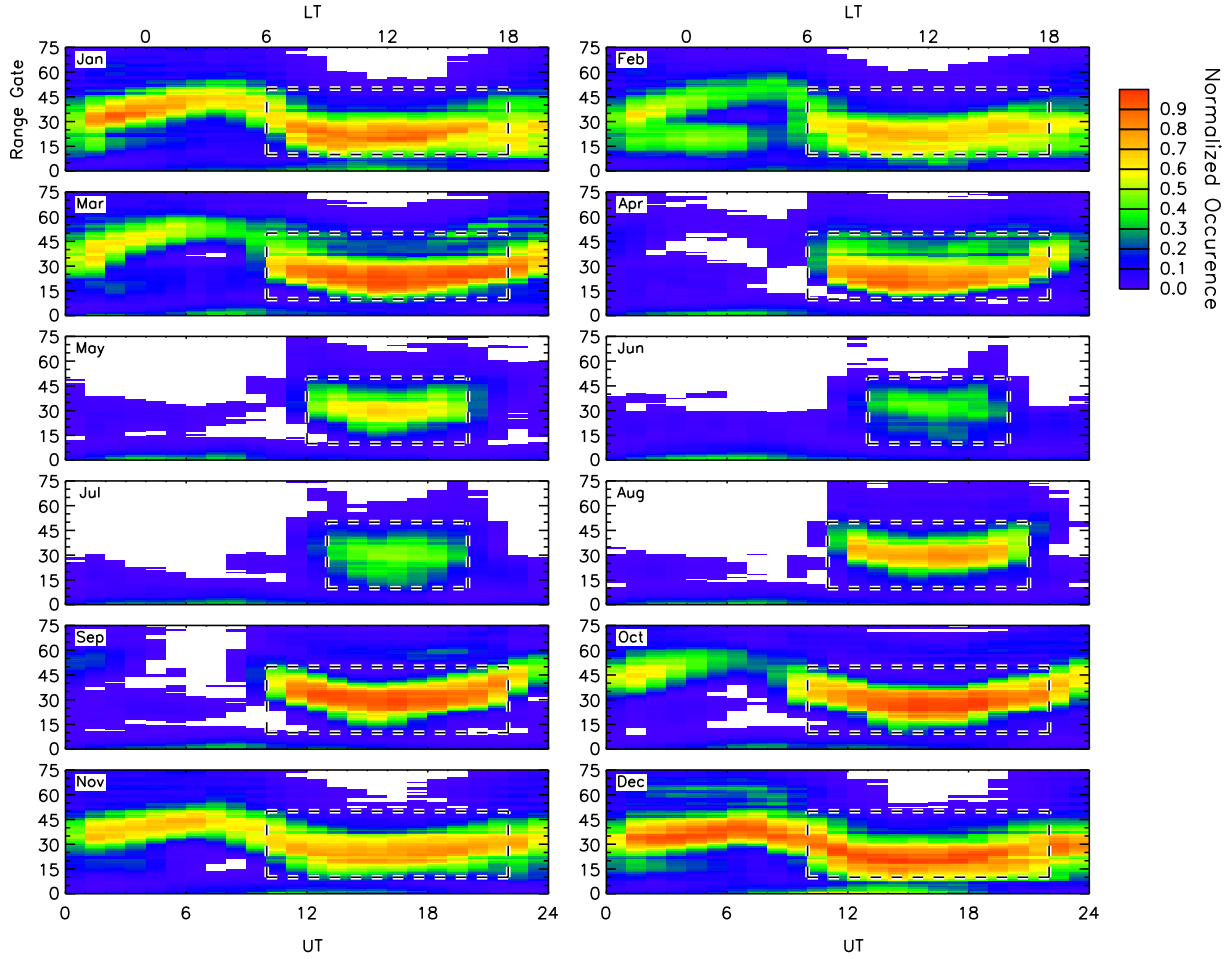


**Figure 5.** Hourly averages of ground-backscatter occurrence, broken down by month and plotted versus radar range gate and universal time, on a normalized occurrence scale indicated by the color bar on the right. Data are shown from the time interval May 2010 to April 2011. The region enclosed by the dashed line on each panel is illustrative of typical regions chosen for MSTID analysis and corresponds to local daytimes and radar ranges 10–50.

[12] The large gap in the results in the second, third, and fourth panels of Figure 4a (from  $\sim 17:00$  to  $18:40$  UT) highlights the need to examine multiple locations in the radar field-of-view. It is quite apparent that TID signatures exist in the first panel throughout most of the interval, but these will not necessarily be identified continuously in any one given radar cell. In this example, during the latter part of the interval, the further range gate (indicated by the upper magenta lines in Figure 4a) can be seen to skirt the upper edge of the MSTID signature, resulting in the observed data gap. By examining a larger number of cells, we can build up a more complete picture of the TID characteristics. In Figure 4b, we present the data from beam 6 of the radar and show the MULMEM results from all corresponding 3-cell sets superposed. This reveals a more continuous set of observations, with some smaller-scale variability. In this case, the observations of wave period, for example, appear to cluster around  $\sim 50$ – $60$  min over much of the observation window, with the occasional identification of a much lower period in very limited observations. These results indicate that while MSTID signatures are clearly evident in the overall picture

provided by the radar data, they do not take the form of simple wavelike perturbations at the radar cell level, nor are they uniform over the entire radar field-of-view. The nature of the radar data is quite complex and the MSTID signatures they contain are similarly so. This serves to illustrate that attempting to make a simple, unique, classification of the MSTID propagation characteristics for an extended interval of observations is therefore not appropriate. Instead, we perform a filtering of the MULMEM results prior to compiling our statistics by considering  $10\text{ min} \times Z$  bins of each parameter, where  $Z$  is equal to  $5\text{ min}$ ,  $20\text{ m s}^{-1}$ ,  $40\text{ km}$ , or  $18^\circ$ , for period, speed, wavelength, and azimuth, respectively. These bins are shown in Figure 4b by the grey grid on each of the second, third, and fourth panels. The purpose of this filtering is twofold: on the one hand, rejection of sparsely populated bins enables “weak” MSTID candidates (i.e., where a positive MULMEM result is returned for a very short time and/or in a very limited portion of the radar field-of-view) to be discarded. At the same time, it minimizes the likelihood that the same MSTID will be counted twice in the statistics simply because it was observed in multiple radar cells.

### 3. Observations

[13] In this section, we discuss a statistical analysis of MSTID observations made by the FIR during the first full year of operations, from 1 May 2010 to 30 April 2011.

#### 3.1. FIR Ground-Backscatter Observations

[14] As discussed above, SuperDARN radars do not make direct observations of TIDs, but instead, observe variations in ground backscatter in which the signatures of the TIDs are apparent. It is therefore prudent to discuss first the basic nature of the radar ground backscatter before considering the observations of MSTIDs. Figure 5 presents hourly averages of ground-backscatter occurrence, broken down by month and plotted versus radar range gate and universal and local time, on a normalized occurrence scale indicated by the color bar on the right. These results show that, during the summer months, a reasonably consistent band of ground backscatter exists whose average range varies modestly with UT/LT, moving away from the radar during the night and back toward the radar during the morning hours, associated with changes in ionospheric density [Milan et al., 1997]. During the winter months, the amount of nighttime scatter decreases, leaving only a patch  $\sim 6$  h in extent centered about local midday present the whole year around.

[15] From our analysis of the radar ground-backscatter characteristics, we define the universal time and radar range limits over which the MULMEM analyses are conducted. The region enclosed by the dashed line on each panel of Figure 5 illustrates typical examples of these limits, although we define the actual UT limits used on a daily basis. Radar ranges below range 10 are likely to contain scatter propagating via the  $E$  region. In order to restrict our analysis to  $F$  region propagation paths, allowing for a simple mapping of the ground-scattered echoes to the ionosphere as described in section 2, we therefore discard all data from below range 10. During the daytime hours, scatter is generally observed up to range 50, which is just beyond the upper range limit discussed in section 2. For reference, these ranges are also indicated in Figure 1 by the thick dashed line (ground range) and thick solid line (mapped range).

[16] As well as the variations with UT, radar range, and season, shorter timescale variations also exist. This short timescale variability is evident in Figure 6a, which presents the daily variation in observed radar ground backscatter plotted as a percentage of the total possible amount of scatter present between 6 and 18 UT, and between radar range gates 10 and 50. This highlights both the longer timescale seasonal variations and shorter timescale variations occurring from day to day. Since the MSTID signatures we are interested in occur within the ground backscatter, the amount of scatter present during a given interval will play a critical role in determining the observed occurrence of MSTIDs, as will be discussed below.

#### 3.2. MSTID Observations

[17] To investigate the occurrence of MSTIDs observed by the FIR, the analysis described in section 2 has been applied systematically to the 12 month period 1 May 2010 to 30 April 2011. An indication of how the amount of ground backscatter observed on any day effects the likelihood of MSTID signatures being observed is shown in Figure 6b,

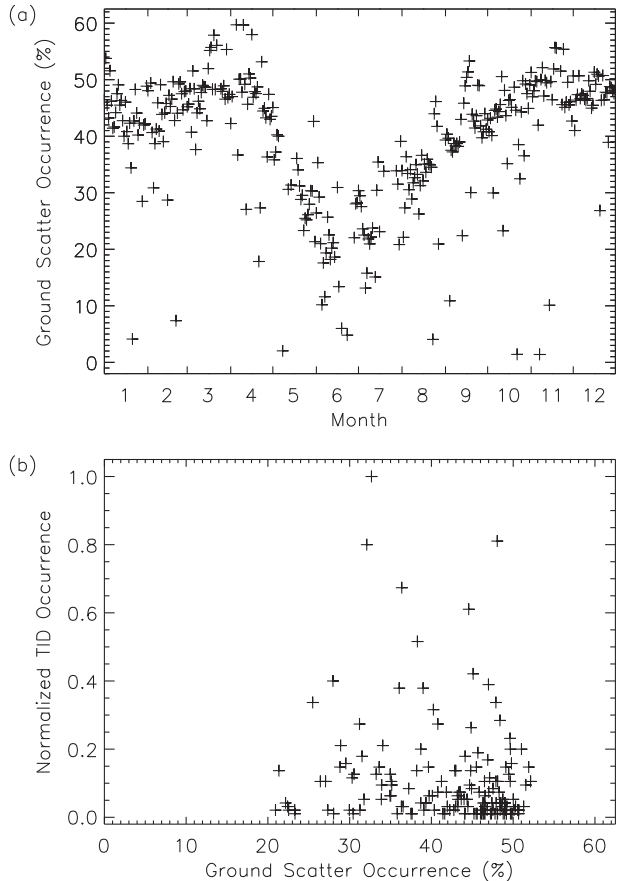


**Figure 6.** (a) Daily occurrence of radar ground backscatter as a percentage of the maximum possible amount of scatter received between 06 and 18 UT, and between range gates 10 and 50. (b) The percentage from Figure 6a plotted versus the normalized daily occurrence of MSTID observations.

which presents the ground-backscatter occurrence percentage from Figure 6a plotted versus the normalized occurrence of MSTID signatures observed on each day. These data show that for ground-backscatter occurrence below about 20%, no MSTID signatures are observed. For ground-backscatter occurrence between about 20% and 40%, the maximum number of MSTID observations possible increases (although days still exist where few or zero MSTIDs were observed). Above about 50% ground-backscatter occurrence, the number of MSTIDs observed drops rapidly to zero. This is due to the combined seasonal dependences of ground-backscatter and MSTID occurrence, discussed below.

[18] Figure 7 presents a set of histograms of the normalized occurrence distributions of various MSTID characteristics. The black lines represent the distribution of the full population, the blue line represents a secondary population discussed below. Figure 7a shows the occurrence versus month and indicates a seasonal dependence of MSTID occurrence. The greatest occurrence is observed around equinox, with minima in summer and winter. In order to address whether these variations are related to the seasonal variation in ground-backscatter occurrence noted above, monthly averages of the ground-backscatter occurrence from Figure 6a (shown here by the plus symbols) have

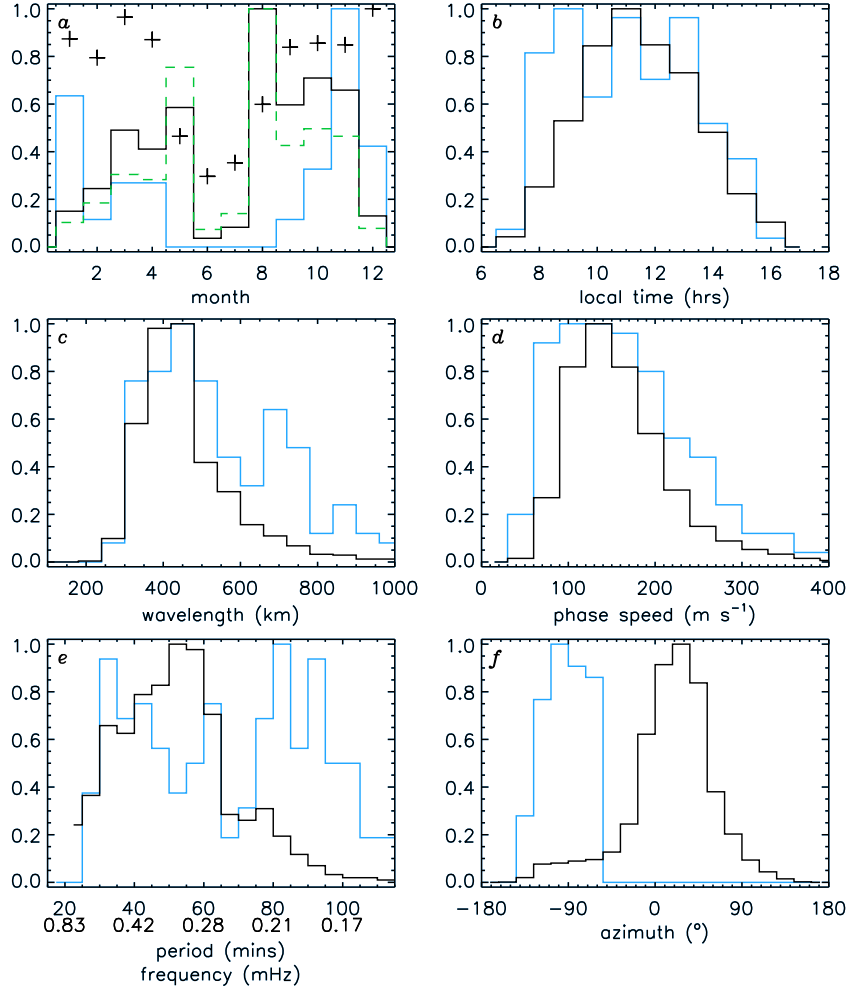


**Figure 7.** Normalized occurrence distributions of MSTID characteristics: (a) month, (b) local time, (c) wavelength, (d) phase speed, (e) period/frequency, and (f) propagation azimuth, for the full population (black) and a secondary population (blue) described in the text. In Figure 7a, the plus symbols show monthly averages of the ground-backscatter occurrence from Figure 6a, and the dashed-green line show a groundscatter-normalized MSTID occurrence.

been used to produce a groundscatter-normalized MSTID occurrence (shown dashed-green). It is still difficult to discern whether the winter minimum corresponds to a real drop in MSTID occurrence, or to the severe reduction in radar ground backscatter that would reduce the ability of the radars to reveal MSTID signatures. The reduction in summer, however, occurs despite the occurrence of ground backscatter being consistently high. We discuss this further in section 4.

[19] Figure 7b shows the occurrence versus local time. The time of an observed MSTID is defined as the midpoint of the dynamic spectral window. As described in section 2, the window is 160 min long and is moved over a maximum interval of 6–18 LT. Therefore, recorded observations are possible from 07:20 to 16:40 LT, and thus, it is data from within this range that are included here. The full distribution consists of a clear single maximum at ~11 LT. While it is expected that the occurrence of MSTID should drop off away from noon, it is also worth noting that, in the winter months at least, the reduction of radar ground-backscatter away from noon will likely also play a role.

[20] Figures 7c–7f present the normalized occurrence distributions of the spectral and propagation characteristics of the MSTIDs. Figure 7c shows the wavelength, which varies between 200 and 800 km, and has a peak occurrence at about 400 km. Figure 7d shows the phase speed of the disturbances in the range 100 to 300 m s<sup>-1</sup>, with a peak occurrence at about 150 m s<sup>-1</sup>. It is worth reiterating that the horizontal wavelength and phase speed are dependent on the choice of mapping used ( $D = 0.6R$ ), and we discuss the effects of changing this in section 4. Figure 7e shows the period (and frequency) distribution, which ranges between ~20 and 100 min (~0.2–0.8 mHz) and peaks at 50 to 60 min (~0.3 mHz). Small, secondary peaks are also apparent at ~30 and ~80 min (~0.6 and ~0.2 mHz). Lastly, Figure 7f shows the distribution of propagation azimuths observed, which are largely equatorward (northward, where  $|\theta| < 90^\circ$ ) with a modest eastward component ( $\theta > 0^\circ$ ).

[21] A more detailed inspection of the radar observations over the study interval revealed a small population of MSTIDs at near-radar ranges (within ~500 km of the radar), with a strong westward propagation component (azimuths

within  $-144^\circ > \theta > -54^\circ$ ). Evidence for this population can be seen in Figure 7f as a sustainment of the leading edge of the parent distribution around  $-90^\circ$ . Using the range and azimuth limits mentioned above, this population has been extracted from, and scaled to, the parent population and is shown in blue in all panels of Figure 7. Besides the azimuth, the most significant difference between this population and the parent population is the seasonal dependence, which in this case shows a strong bias toward summer. A somewhat broader, or multipeaked, distribution of TID period is also revealed, with a corresponding broadening of the wavelength distribution. The significance of these events is discussed in more detail in section 4.

#### 4. Discussion

[22] The MSTID characteristics discussed above are consistent with the results of previous studies at different geographical locations [e.g., *Bristow et al.*, 1994, 1996; *He et al.*, 2004; *Kotake et al.*, 2007]; a generally equatorward and eastward propagation direction in the main population, with periods of a few tens of minutes to an hour and wavelengths of a few hundred km. The diurnal variation is also as expected, with a peak close to local noon (Figure 7b). The seasonal variation suggests that most MSTIDs occurred around equinox (Figure 7a). The lack of any significant population in winter (June and July) would appear to be due to the low level of radar ground-backscatter occurrence. Indeed, when the backscatter level goes significantly above the  $\sim 20\%$  threshold in August (Figure 6), the MSTID occurrence increases sharply (Figure 7a). However, although high occurrences of MSTIDs have been observed at high latitudes in winter [e.g., *Ogawa et al.*, 1987], *Hirota* [1984] found that gravity wave activity at lower latitudes shows a maximum around the equinoxes. If the MSTIDs revealed by our observations are due to AGW, then this could also be a factor in the seasonal variation. The lack of a significant summer population, on the other hand, is consistent with the results of many previous studies of daytime MSTIDs [e.g., *Ogawa et al.*, 1987; *Kotake et al.*, 2007]. In the summer, the level of ground backscatter is high, and therefore, the reduction in MSTID observations during December and January is likely to be real.

[23] One open question concerns the relationship between MSTIDs and geomagnetic activity. Some earlier studies, focusing at higher magnetic latitudes, have suggested a close causal relationship between solar wind-magnetosphere-ionosphere (SW-M-I) coupling and MSTID occurrence [e.g., *Huang et al.*, 1998; *Sofko and Huang*, 2000]. *Samson et al.* [1990] suggested that MSTIDs at high latitudes were likely to be related to Earth-reflected AGW produced by Lorentz forcing or Joule heating of the atmosphere. The FIR is located at a considerably lower latitude than the radars used by *Samson et al.*, [1990] and *Bristow et al.* [1994], such that MSTIDs associated with an auroral source would have to propagate over considerable distances ( $\sim 3000$  km) to be detected in our case. Although *Francis* [1974] demonstrated that MSTIDs induced by Earth-reflected AGW can propagate over long distances, the propagation range is proportional to wavelength. Consequently, shorter wavelength MSTIDs propa-

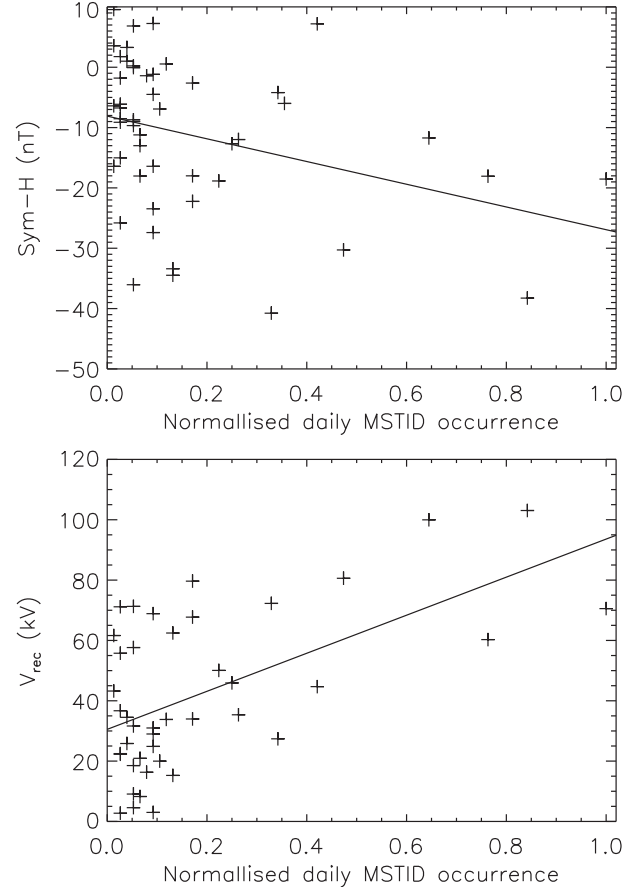


**Figure 8.** Scatter plots of normalized daily MSTID occurrence versus the (top) dayside Sym-H index and (bottom) dayside reconnection voltage. Linear best fit lines are superposed in each case.

gating from an auroral source may be expected to dissipate before reaching the midlatitudes. However, as discussed by *Mayr et al.* [1990], an alternative wave mode which is ducted between the Earth's surface and the lower thermosphere exists. The ducted AGWs propagate to lower latitudes through the nondissipative lower atmosphere, where they "leak" into the thermosphere and produce a MSTID. However, as pointed out by *Hocke and Schlegel* [1996], it is nontrivial to relate midlatitude MSTIDs to high-latitude sources because medium-scale waves are also excited by sources in the lower atmosphere by wind shears or orography. It has been postulated that near to the Antarctic Peninsula, for example, MSTIDs may be associated with AGW directly excited by winds over the Andean and Antarctic Peninsula mountains [*Alexander et al.*, 2008] or by the high winds of the Antarctic Polar Vortex [*Ern et al.*, 2004].

[24] To investigate the relationship between our observations of MSTIDs and SW-M-I coupling, we compared the normalized daily occurrence of MSTIDs (from Figure 6b) with (a) Sym-H index and (b) the dayside reconnection voltage ( $V_{rec}$ ), as shown in Figure 8. Sym-H is a measure of the strength of the symmetric ring current [Iyemori and Rao, 1996] and represents the integrated effects of SW-M-I coupling, whereas  $V_{rec}$ , derived from upstream interplanetary data [Milan et al., 2012], provides a more direct measure of

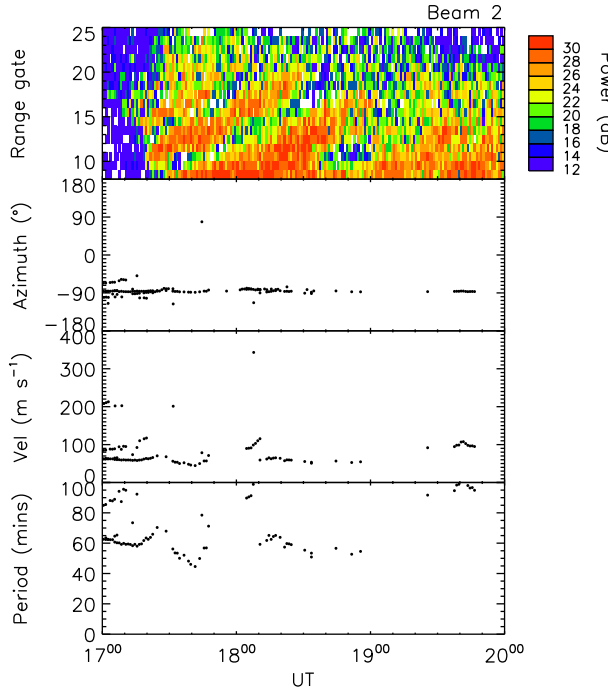


**Figure 9.** One example set of MSTID observations, from 29 January 2011, in a similar format to Figure 4b.

solar wind driving. We focus on 6 months of observations around the equinoxes (March–May and August–October) and use 4 h averages of both Sym-H and  $V_{rec}$ . The results of a Pearson correlation analysis revealed that the strongest relationship with Sym-H ( $r = -0.33$ ) occurred for Sym-H averaged over 09:20–13:20 UT (05:20–09:20 LT) and with  $V_{rec}$  ( $r = 0.57$ ) for  $V_{rec}$  averaged over 10:30–14:30 UT (06:30–10:30 LT). Although relatively weak correlations, these results do suggest a degree of association between MSTID occurrence and the level of SW-M-I coupling, and could provide evidence for the ducted mode of propagation from a high-latitude source as discussed above. The stronger correlation for  $V_{rec}$  is consistent with these dayside MSTIDs occurring in direct response to solar wind-magnetosphere coupling at the dayside magnetopause, and subsequent Joule heating of the auroral ionosphere, as suggested by Sofko and Huang [2000]. The fact that these MSTIDs propagate approximately equatorward is then also consistent with propagation from auroral to midlatitudes, with persistent propagation parameters, as reported by Ishida *et al.* [2008]. A somewhat weaker correlation with Sym-H is perhaps expected, since Sym-H reflects a general enhancement in geomagnetic activity that will, at least in part, be associated with substorm activity in the tail. Sym-H might therefore be expected to correlate better with nightside MSTID occurrence (e.g., S. E. Milan *et al.*, Travelling ionospheric disturbances in the Weddell Sea anomaly associated with geomagnetic activity, submitted to *Journal of Geophysical Research*, 2013).

[25] In section 3.2, we identified a secondary population of MSTIDs, observed at near-radar ranges, that exhibited a strongly westward propagation direction (blue lines in Figure 7) and occurred predominantly in the summer. An

example of such an event is illustrated in Figure 9, which shows the backscattered power from the westward-pointing radar beam 2, and the MSTID propagation azimuth, velocity, and period, in a similar format to Figure 4b. In this case, the MSTID was only evident over a relatively short  $\sim 2$  h interval, so we have shortened the time-axis accordingly. Although the data are somewhat sparser than those in Figure 4b, owing to the restricted number of range gates over which these near-range observations were made, a dominant signature is still evident in the data. The key difference between this near-range event and those typical of the parent population (illustrated in Figure 4) is in the alignment of the power striations, which in this case imply a modest propagation away from the radar. The azimuth (second panel) is revealed to have been consistently  $-90^\circ$  (westward), in line with previous studies of upward propagating summertime atmospheric gravity waves [e.g., Moffat-Griffin *et al.*, 2011].

[26] If this secondary population represents MSTIDs generated by AGW propagating upward from the troposphere, its low occurrence could be due to the likelihood that most AGW of tropospheric origin will not reach the thermosphere due to wave breaking and the filtering effects of winds [e.g., Francis, 1974]. Those that are observed could be associated with AGWs excited by winds over the Andean and Antarctic Peninsula mountains or by the high winds of the Antarctic Polar Vortex as suggested above, although we note that the mountain waves discussed by Alexander *et al.* [2008] were only observed during winter, in contrast to our summer time observations. A study by Crowley *et al.* [1987] indicated that MSTID propagation direction was related to the direction of the neutral wind. They indicate that the filtering effect of the winds could result in AGW being reflected, trapped, or penetrating to higher altitudes. In their results, such a filtering effect causes the TID azimuths to cluster around the antiwindward direction. This might explain why, for our secondary population, the predominantly observed TID direction is westward, in a region where winds over the Andes would have an eastward direction. A comparison of coincident observations of the neutral wind with TID characteristics determined by SuperDARN would shed more light on this and is suggested as a topic for future work.

[27] The other parameters of this secondary population that exhibit notable differences compared to the parent population are the period and wavelength. The longer wavelength portion of the distribution (i.e., from 600 to 1000 km) is more consistent with the observations of Ern *et al.* [2004] and Alexander *et al.* [2008], who reported wavelengths from 400 km to in excess of 2000 km. However, it should be pointed out that the satellites used in their studies cannot resolve shorter horizontal wavelengths and that these shorter wavelengths are likely still there. It would therefore appear that the radar is observing MSTIDs associated with a portion of the total AGW population that is missing from the satellite data. If so, a large-scale survey of MSTIDs from all of SuperDARN could provide a valuable resource to future AGW studies. It is worth noting a possible underestimate of MSTID wavelength (and velocity) in our statistics, as a result of the mapping discussed in section 2. To investigate this, we determined the effects of changing the mapping, using the range of realistic alternatives discussed in section 2.1 [Bristow *et al.*, 1994; He *et al.*, 2004; Hall *et al.*, 1999]. We found that the overall

shape of the wavelength and velocity distributions remains largely unchanged, and the peaks of the distributions shift by only  $\sim 100$  km and  $\sim 50$  m s $^{-1}$ , respectively. While this uncertainty does not greatly impact the results of our study, care must be taken in drawing strong conclusions from comparisons between AGW parameters estimated using different techniques and different observational methods.

## 5. Summary

[28] The morphology of MSTIDs, observed near to the Antarctic Peninsula by HF radar, has been presented. The distribution of MSTID periods was found to span 30–60 min, corresponding to frequencies of 0.3–0.6 mHz. Wavelengths were generally in the range 200–800 km and phase speeds in the range 100–300 m s $^{-1}$ . A primary population of northward (equatorward) propagating MSTIDs was observed, mainly at the equinoxes, with peak daily occurrences during intervals of enhanced solar wind-magnetosphere coupling as evidenced by estimates of the concurrent dayside reconnection voltage. Also observed was a smaller, westward propagating population that could be associated with AGWs excited by winds over the Andean and Antarctic Peninsula mountains or by the high winds of the Antarctic Polar Vortex, that propagate up from the troposphere. A number of further studies are suggested by the results of our investigation. A comparison of MSTIDs simultaneously observed by different instrumentation and techniques would enable the mapping uncertainty present in the SuperDARN analysis to be determined. A large-scale study of coincident observations of the neutral wind and MSTID characteristics observed by SuperDARN would help elucidate the factors governing MSTID propagation direction. The technique described here, if applied to the entire archive of data from the full SuperDARN array, could provide a wealth of information on hemispheric and latitudinal differences in MSTID activity over solar cycle timescales.

[29] **Acknowledgments.** Construction of the FIR, and support for MPF, was funded by NERC grant NE/G018707/1. A.G. and S.E.M. were supported by NERC grant NE/G019665/1. A.G. was also supported by a JSPS Invitation Fellowship (grant L11521) during part of this study. A.G. thanks Terry Robinson for helpful discussions on gravity wave theory.

[30] Robert Lysak thanks the reviewers for their assistance in evaluating this paper.

## References

- Alexander, M. J., et al. (2008), Global estimates of gravity wave momentum flux from high resolution dynamics limb sounder observations, *J. Geophys. Res.*, 113, D15S18, doi:10.1029/2007JD008807.
- Bristow, W. A., R. A. Greenwald, and J. C. Samson (1994), Identification of high-latitude acoustic-gravity wave sources using the Goose Bay HF radar, *J. Geophys. Res.*, 99(A1), 319–331.
- Bristow, W. A., R. A. Greenwald, and J.-P. Villain (1996), On the seasonal dependence of medium-scale atmospheric gravity waves in the upper atmosphere at high latitudes, *J. Geophys. Res.*, 101(A7), 15,685–15,699, doi:10.1029/96JA01010.
- Chimonas, G., and C. O. Hines (1970), Atmospheric gravity waves launched by auroral currents, *Planet. Space Sci.*, 18(4), 565–582, doi:10.1016/0032-0633(70)90132-7.
- Chisham, G., et al. (2007), A decade of the Super Dual Auroral Radar Network (SuperDARN): Scientific achievements, new techniques and future directions, *Surv. Geophys.*, 28, 33–109, doi:10.1007/s10712-007-9017-8.
- Crowley, G., T. B. Jones, and J. R. Dudney (1987), Comparison of short-period TID morphologies in Antarctica during geomagnetically quiet and active intervals, *J. Atmos. Terr. Phys.*, 49(11–12), 1155–1162, doi:10.1016/0021-9169(87)90098-5.
- Eckermann, S. D. (1992), Ray tracing simulation of the global propagation of inertia gravity-waves through the zonally averaged middle atmosphere, *J. Geophys. Res.*, 97(D14), 15,849–15,866.
- Ern, M., P. Preusse, M. J. Alexander, and C. D. Warner (2004), Absolute values of gravity wave momentum flux derived from satellite data, *J. Geophys. Res.*, 109, D20103, doi:10.1029/2004JD004752.
- Evans, J. V., J. M. Holt, and R. H. Wand (1983), A differential-Doppler study of travelling ionospheric disturbances from Millstone Hill, *Radio Sci.*, 18, 435–451.
- Francis, S. H. (1974), A theory of medium-scale travelling ionospheric disturbances, *J. Geophys. Res.*, 79(34), 5245–5260, doi:10.1029/JA079i034p05245.
- Greenwald, R. A., et al. (1995), Darn/SuperDarn: A global view of the dynamics of high-latitude convection, *Space Sci. Rev.*, 71, 761–796, doi:10.1007/BF00751350.
- Hall, G., J. MacDougall, J. Cecile, D. Moorcroft, and J. St-Maurice (1999), Finding gravity wave source positions using the super dual auroral radar network, *J. Geophys. Res.*, 104(A1), 67–78.
- He, L.-S., P. L. Dyson, M. L. Parkinson, and W. Wan (2004), Studies of medium scale travelling ionospheric disturbances using TIGER SuperDARN radar sea echo observations, *Ann. Geophys.*, 22(12), 4077–4088.
- Hines, C. O. (1960), Internal atmospheric gravity waves at ionospheric heights, *Can. J. Phys.*, 38, 1441–1481.
- Hirota, I. (1984), Climatology of gravity-waves in the middle atmosphere, *J. Atmos. Terr. Phys.*, 46(9), 767–773, doi:10.1016/0021-9169(84)90057-6.
- Hocke, K., and K. Schlegel (1996), A review of atmospheric gravity waves and travelling ionospheric disturbances: 1982–1995, *Ann. Geophys.*, 14(9), 917–940, doi:10.1007/s005850050357.
- Hooke, W. H. (1968), Ionospheric irregularities produced by internal atmospheric gravity waves, *J. Atmos. Terr. Phys.*, 38, 795–829.
- Huang, C., D. Andre, and G. Sofko (1998), Observations of solar wind directly driven auroral electrojets and gravity waves, *J. Geophys. Res.*, 103(A10), 23,347–23,356.
- Ishida, T., K. Hosokawa, T. Shibata, S. Suzuki, N. Nishitani, and T. Ogawa (2008), Superdarn observations of daytime mstids in the auroral and mid-latitudes: Possibility of long-distance propagation, *Geophys. Res. Lett.*, 35, L13102, doi:10.1029/2008GL034623.
- Iyemori, T., and D. R. K. Rao (1996), Decay of the *Dst* field of geomagnetic disturbance after substorm onset and its implication to storm-substorm relation, *Ann. Geophys.*, 14(6), 608–618.
- Kelley, M. C., and C. A. Miller (1997), Electrodynamics of midlatitude spread F3. Electrodynamical waves? A new look at the role of electric fields in thermospheric wave dynamics, *J. Geophys. Res.*, 102(A6), 11,539–11,547, doi:10.1029/96JA03841.
- Kotake, N., Y. Otsuka, T. Ogawa, T. Tsugawa, and A. Saito (2007), Statistical study of medium-scale traveling ionospheric disturbances observed with the GPS networks in Southern California, *Earth Planets Space*, 59, 95–102.
- MacDougall, J. W., D. A. Andre, G. J. Sofko, C. S. Huang, and A. V. Koustov (2001), Travelling ionospheric disturbance properties deduced from super dual auroral radar measurements, *Ann. Geophys.*, 18(12), 1550–1559, doi:10.1007/s005850000293.
- Mayr, H. G., I. Harris, F. A. Herrero, N. W. Spencer, F. Varosi, and W. D. Pesnell (1990), Thermospheric gravity-waves—Observations and interpretation using the transfer-function model (TFM), *Space Sci. Rev.*, 54(3–4), 297–375.
- Milan, S. E., T. K. Yeoman, M. Lester, E. C. Thomas, and T. B. Jones (1997), Initial backscatter occurrence statistics from the CUTLASS HF radars, *Ann. Geophys.*, 15(6), 703–718.
- Milan, S. E., J. S. Gosling, and B. Hubert (2012), Relationship between interplanetary parameters and the magnetopause reconnection rate quantified from observations of the expanding polar cap, *J. Geophys. Res.*, 117, A03226, doi:10.1029/2011JA017082.
- Miller, C. A., W. E. Swartz, M. C. Kelley, M. Mendillo, D. Nottingham, J. Scali, and B. Reinisch (1997), Electrodynamics of midlatitude spread F1. Observations of unstable, gravity wave-induced ionospheric electric fields at tropical latitudes, *J. Geophys. Res.*, 102(A6), 11,521–11,532, doi:10.1029/96JA03839.
- Moffat-Griffin, T., R. E. Hibbins, M. J. Jarvis, and S. R. Colwell (2011), Seasonal variations of gravity wave activity in the lower stratosphere over an Antarctic Peninsula station, *J. Geophys. Res.*, 116, D14111, doi:10.1029/2010JD015349.
- Ogawa, T., K. Igarashi, K. Aikyo, and H. Maeno (1987), NNSS Satellite-observations of medium-scale traveling ionospheric disturbances at southern high-latitudes, *J. Geomagn. Geoelec.*, 39(12), 709–721.
- Otsuka, Y., K. Shiokawa, T. Ogawa, and P. Wilkinson (2004), Geomagnetic conjugate observations of medium-scale traveling ionospheric disturbances at midlatitude using all-sky airglow imagers, *Geophys. Res. Lett.*, 31, L15803, doi:10.1029/2004GL020262.

- Perkins, F. (1973), Spread F and ionospheric currents, *J. Geophys. Res.*, 78(1), 218–226, doi:10.1029/JA078i001p00218.
- Samson, J. C., R. A. Greenwald, J. M. Ruohoniemi, and K. B. Baker (1989), High-frequency radar observations of atmospheric gravity-waves in the high-latitude ionosphere, *Geophys. Res. Lett.*, 16(8), 875–878.
- Samson, J. C., R. A. Greenwald, J. M. Ruohoniemi, A. Frey, and K. B. Baker (1990), Goose bay radar observations of earth-reflected, atmospheric gravity-waves in the high-latitude ionosphere, *J. Geophys. Res.*, 95(A6), 7693–7709.
- Shibata, T. (1987), Application Of multichannel maximum-entropy spectral-analysis to the HF Doppler data Of medium-scale TID, *J. Geomagn. Geoelec.*, 39(5), 247–260.
- Shiokawa, K., C. Ihara, Y. Otsuka, and T. Ogawa (2003), Statistical study of nighttime medium-scale traveling ionospheric disturbances using midlatitude airglow images, *J. Geophys. Res.*, 108(A1), 1052, doi:10.1029/2002JA009491.
- Sofko, G. J., and C. S. Huang (2000), Superdarn observations of medium-scale gravity wave pairs generated by joule heating in the auroral zone, *Geophys. Res. Lett.*, 27(4), 485–488.
- Strand, O. N. (1977), Multichannel complex maximum entropy (autoregressive) spectral analysis, *IEEE Trans. Autom. Control*, 22(4), 634–640, doi:10.1109/TAC.1977.1101545.
- Ulrych, T. J., and T. N. Bishop (1975), Maximum entropy spectral analysis and autoregressive decomposition, *Rev. Geophys.*, 13(1), 183–200, doi:10.1029/RG013i001p00183.